# Effects of a magnetic field on hot electron generation from laser-plasma instabilities

Cite as: Phys. Plasmas 33, 022503 (2026); doi: 10.1063/5.0308625
Submitted: 23 October 2025 · Accepted: 22 January 2026 ·
Published Online: 10 February 2026



E. Rovere,[1,a] R. K. Follett,[2] F. S. Tsung,[3] B. J. Winjum,[3] J. J. Santos,[4] G. Pérez-Callejo,[5] R. Florido,[6] A. Bordón-Sanchez,[6] M. Caetano de Sousa,[4] M. A. Gigosos,[5] F. N. Beg,[1] and M. Bailly-Grandvaux[1,b]

## AFFILIATIONS

[1]Center for Energy Research, University of California-San Diego, La Jolla, California 92093, USA
[2]Laboratory for Laser Energetics, University of Rochester, Rochester, New York 14623, USA
[3]Institute for Digital Research and Education, University of California Los Angeles, Los Angeles, California 90095, USA
[4]Centre Lasers Intenses et Applications (CELIA), Université de Bordeaux-CNRS-CEA, UMR 5107, F-33405 Talence, France
[5]Departamento de Física Teórica Atómica y Óptica, Universidad de Valladolid, 47011 Valladolid, Spain
[6]iUNAT-Departamento de Física, Universidad de Las Palmas de Gran Canaria, 35017 Las Palmas de Gran Canaria, Spain

[a]Author to whom correspondence should be addressed: erover@ucsd.edu
[b]Electronic mail: mbaillygrandvaux@ucsd.edu

## ABSTRACT

We performed two-dimensional simulations of turbulent laser-plasma instabilities in the presence and absence of external magnetic fields using the Laser Plasma Simulation Environment (LPSE) code. The results demonstrate that, in the presence of a magnetic field, the transition from ballistic to gyrating electron motion enhances the energy transfer from electron plasma waves to the electron population. Although stronger magnetic fields produce a larger population of hot electrons, these electrons tend to remain confined near the quarter-critical density, where the instabilities also localize, thereby reducing the potential for hot electron transport deeper into the target. Additionally, we present a scaling analysis that quantifies hot electron generation as a function of plasma electron temperature, density scale length, and applied magnetic field strength. These findings may have important applications for controlling hot electron flux and mitigating preheat in inertial confinement fusion targets.





## I. INTRODUCTION

Strong nonlinear coupling between a laser drive and a plasma arises when the laser drive is in the range of $I\lambda_0^2 \sim 10^{13}-10^{16}\mathrm{W}\mu\mathrm{m}^2/\mathrm{cm}^2$ and pulse durations the order of $0.1-10\mathrm{ns}$ (where I is the laser intensity and $\lambda_0$ is the laser wavelength in $\mu$m). This coupling leads to the onset of laser-plasma instabilities (LPIs), including three-wave decay processes,[1,2] resonant absorption,[3] filamentation,[4–6] self-focusing,[7] and strong plasma turbulence.[8–10] In a three-wave decay process, a "mother" wave decomposes into two "daughter" waves up to the plasma critical density $n_c = 1.1 \times 10^{21}/\lambda_{0,\mu m}^2 \mathrm{cm}^{-3}$,[11] obeying matching conditions both in wave number (conservation of momentum) and frequency (conservation of energy).[12] The most relevant three-wave decays are Stimulated Raman Scattering (SRS),[13–15] Two-Plasmon Decay (TPD),[16–18] Stimulated Brillouin Scattering (SBS),[19] and Langmuir Decay Instability (LDI).[20–22] Moreover, "strong" Langmuir turbulence, also referred to as Langmuir wave (LW) collapse or cavitation, can be generated by low-wavenumber electron plasma waves (EPWs) from LDI cascade.[8,23,24] These LPIs play a central role in inertial confinement fusion (ICF) schemes,[25,26] where they can divert laser energy away from the target and/or drive the production of hot electrons (HEs). While HEs can enhance shock compression and benefit certain ICF designs,[27] they can cause detrimental preheating of the target.[28] Thus, understanding and controlling LPIs is essential for achieving optimal performance in ICF experiments.

In parallel, magnetized inertial fusion (MIF) schemes,[29–33] the role of self-generated magnetic fields in non-ideal direct-drive ICF,[34] as well as magnetized plasma dynamics in Z-pinch machines,[35–37] are attracting growing research interest. ICF implosions are typically fast enough that magnetic B-field lines are "frozen-in" to the compressing target,[38] amplifying a seed field of $1-10\,\mathrm{T}$ to values of $10^3-10^4\,\mathrm{T}$. This amplified B-field enhances $\alpha$ particle confinement and suppresses

heat transport perpendicular to the magnetic field,[39–41] thereby relaxing ignition constraints. In addition, magnetic tension can also influence hydrodynamic instabilities.[42,43]

While significant attention has been devoted to the core dynamics of magnetized imploding targets, comparatively few studies have examined the effects of magnetic fields on HE-generating LPIs within the coronal plasma. Early theoretical work by Sagdeev and Shapiro[44] and Dawson *et al.*[45] explored fundamental aspects of magnetized wave dynamics, while more recent studies by Winjum *et al.*,[46] Yao *et al.*,[47] and Li *et al.*[48] investigated specific LPI mechanisms in detail. In particular, Refs. 46 and 47 analyzed the impact of magnetic fields on low-density SRS subject to spatial amplification, whereas[48] focused on TPD near $n_c/4$.

The objective of this work is to extend previous studies of LPI and HE generation in the presence of a magnetic field, building on earlier investigations.[46–48] To this end, we employ the hybrid simulation code Laser Plasma Simulation Environment (LPSE) to examine instabilities arising near quarter-critical density ($n_c/4$), including SRS, TPD, LDI, and plasma turbulence. Our simulations show that applying a B-field reduces EPW activity, increases the HE population, and decreases the HE energy flux perpendicular to the B-field direction. In contrast to previous studies,[46–48] we survey a wider parameter space—electron temperature, density scale length $L_n \equiv (\partial \ln n_e/\partial x)^{-1}$, and magnetic field strength—to systematically assess the influence of the B-field on LPIs around $n_c/4$. A key novelty of this work is the explicit inclusion of plasma turbulence (LDI and LW collapse), which, to the best of our knowledge, has not been considered in prior studies, enabling a more comprehensive view of magnetized LPI evolution at $n_c/4$.

The results of this work suggest that preheat of ICF targets by hot electrons could be mitigated in unstable regions where applied or self-generated B-fields persist perpendicular to the laser drive. Conversely, in Magnetized Liner Inertial Fusion (MagLIF) experimental platforms,[33,36] the imposed axial magnetic field enhances heat confinement by guiding the HEs along the cylinder target axis, enabling more efficient laser preheating of the plasma prior to liner implosion.

The organization of this paper is as follows. Section II describes the LPSE simulation code and the parameter sets employed. Section III presents differences in activity and field structure for electron plasma waves, ion acoustic waves, and Raman light between unmagnetized and magnetized (30 T) cases. Section IV provides an estimate of the B-field's impact on individual LPIs by analyzing laser transmissivity. Finally, Sec. V focuses on differences in electron motion and HE generation and presents a preliminary exploration of how magnetic field strength influences outcomes while varying the plasma electron temperature and density scale length.

## II. SIMULATION SETUP

To investigate the effect of a magnetic field on LPIs (here including SRS, TPD, LDI, and LW collapse) near quarter-critical density, we used the hybrid fluid code Laser Plasma Simulation Environment (LPSE).[49,50] LPSE solves a set of time-enveloped field equations for laser light, Raman light, and EPWs, while ion acoustic waves (IAWs) are treated with linearized hydrodynamic equations.[14] Both EPW and IAW responses are linearized for small perturbations relative to the background density. The code allows investigation of individual LPIs, such as SRS or TPD, or a combined system in which a single equation incorporates the perturbed electric field representing both EPWs and scattered light. Landau damping is included in the response field and applied in k-space to the longitudinal (electrostatic) part of the field. LPSE also features a kinetic module (hybrid particle evolution, HPE) that tracks virtual macro-particles (the order of $\sim 10^{11}$ electrons per particle) in the evolving EPW field. Particle trajectories evolve under the $\mathbf{E} + \mathbf{v} \times \mathbf{B}$ Lorentz force, and the velocity distribution function (VDF) at each time step is used to calculate the Landau damping coefficient

$$\gamma_{LD}^{EPW}(\boldsymbol{k}, t) = \frac{\pi \omega_{p0}^3}{2k^2} \int d\boldsymbol{v} \cdot \frac{\partial \langle F \rangle(\boldsymbol{v}, t)}{\partial \boldsymbol{v}} \delta(\omega_{p0} - \boldsymbol{k} \cdot \boldsymbol{v}), \tag{1}$$

where $\langle F \rangle(\boldsymbol{v}, t)$ is the spatially averaged VDF.[51]

In the presence of a perpendicular B-field, electron trajectories are influenced not only by the Lorentz force, but also by an oscillation motion that arises when particles become trapped in regions where the EPW field is strongest,[46] close to $n_c/4$. Through this process, electrons gain energy from the EPWs until they reach a detrapping velocity threshold ($v_y = cE_x/B_0$, where $\hat{\mathbf{x}}$ is the direction of laser propagation and $\hat{\mathbf{y}}$ is the direction perpendicular to the laser), at which point they are released from the LPI front with increased energies and a corresponding larger Larmor radius $r_L \equiv mv_y/|q|B_0 \equiv v_y/\omega_c$ (with $\omega_c$ the cyclotron frequency). This phenomenon is known as "surfatron" in plasma-based electron accelerators.[52,53]

We explored different plasma and B-field initial conditions in the LPSE simulations. Electron and ion plasma temperatures of $T_e = 1, 3, 4$ keV and $T_i = 0.33, 1, 1.33$ keV, respectively, and density scale lengths of $L_n = 150, 200, 250$ $\mu$m were studied, with the plasma density profile taken as exponential. For $L_n = 250$ $\mu$m, densities spanned $n_e/n_c = [0.19 - 0.27]$. The case $T_e = 3$ keV, $L_n = 250$ $\mu$m serves as a reference throughout this work for unmagnetized vs magnetized comparisons. For $L_n = 150$ and 200 $\mu$m, density intervals were adjusted to $\simeq [0.16, 0.284]$ and $\simeq [0.177, 0.275]$, respectively, ensuring identical simulation domain sizes and consistent $n_c/4$ positions. This consistency allows equivalent electron sampling from the HPE module across all cases. Simulations covered an $88 \times 10$ $\mu m^2$ domain, with a $4320 \times 490$ grid and approximately 17.2 cells per laser wavelength. The laser was a p-polarized plane wave with vacuum intensity $I = 7 \times 10^{14}$ W/cm$^2$, injected from the low-density boundary. These laser-plasma conditions have been chosen to represent relevant direct-drive ICF conditions for OMEGA,[26] as well as early-MagLIF[54] scenarios. However, this work is mainly focused on three aspects. First, the enveloped EPWs mean that the investigation occurs in a specific density interval near $n_c/4$. While the behavior of TPD and absolute SRS is well described in this interval, the behavior of convective SRS has not been taken into account. Second, the focus has been on p-polarized light, which can influence the dominance of one instability over the others near $n_c/4$. Third, the single beam configuration we adopted means considering a simple model, useful for making a comprehensive parameter scan as in our work, but cannot take into account multi-beam effects.[55] The possibility of exploring different density intervals for convective SRS, a more comprehensive polarization configuration by adding a mixture of both s- and p-polarization, and taking into account multi-beam effects, can be interesting topics for future research. The external magnetic field, $B_{ext}$, was applied uniformly perpendicular to the 2D simulation plane ($\hat{\mathbf{z}}$ direction), ranging from 0 T to 45 T. Normalized cyclotron frequencies $\omega_c/\omega_0$ were $\simeq 2 \times 10^{-3}$; corresponding thermal gyroradii were $r_c \simeq 1.78$ $\mu$m for $T_e = 1$ keV

and $r_c \simeq 3.08\ \mu m$ for $T_e = 3$ keV. Simulation time was set at $t_{sim} = 12$ ps, with a sampling time of $\sim 0.4$ ps. Particles tracked by the HPE module were injected at initialization. Thermalizing boundaries were imposed in the longitudinal ($\hat{x}$) direction, and periodic boundaries in the transverse ($\hat{y}$) direction.

In order to include a physically accurate description not only of LPIs, but also of LW collapse, both the HPE module and Eq. (1) follow the quasi-linear Zakharov model (QZAK) described in Ref. 56. This model follows three main validity conditions, which we verified for our simulation cases. First, the Langmuir wave field must be weak enough so that $|E_{LW^2}/4\pi n_{e,0} T_{e,0}| < 1$, reaching $\sim 10^{-2}$ for the strongest fields recorded in our simulations; second, the Langmuir wave spectrum needs to develop fast enough to prevent particle trapping. Similarly,[56] our simulations show the LW Fourier spectrum develops in a fraction of a picosecond ($\sim$0.4 ps). Finally, the particle population needs to provide a uniform particle distribution so that a global average can be computed. Since the HPE module tracks a population of $\sim 10^6$ in our simulation, this requisite is being satisfied as well.

Unmagnetized simulations typically reach quasi-stationary conditions by $\simeq 5 - 6$ ps. However, since electrons in LPSE do not experience collisions, the B-field can keep the electrons trapped within the simulation domain indefinitely. As a result, for sufficiently long simulation times (40–50 ps), the EPW average energy density in the simulations decreases toward zero due to persisting Landau damping. Estimated electron-ion collision timescales are $\tau_{ei} \simeq 12$ ps for 25 keV electrons and $\tau_{ei} \simeq 31.25$ ps for 50 keV electrons. A 25 keV electron energy corresponds to a thermal velocity that begins to strongly resonate with the EPWs' phase velocity ($v_{ph} \sim 3 - 5 v_{Te}$). A 50 keV electron energy is instead a typical cutoff energy above which the electrons are considered "hot" enough to pose preheat concerns.[26,57] Because 25 keV electron–ion collision timescale is comparable to the simulation time and represents a lower bound for energy deposition, and as the reduction in EPW energy density remains limited by this time, HE production can be considered quasi-stationary over the simulated timescales.

A further consideration is that a sufficiently strong B-field could alter plasma-wave dispersion relations. To assess this, we estimated the ratio of the cyclotron frequency ($\omega_c$) to the plasma frequency ($\omega_p$). For a $\lambda_0 = 0.351\ \mu$m laser and a $T_e = 3$ keV plasma with applied B-fields of 15 and 45 T, evaluated at quarter critical density ($n_c/4$), the respective ratios are $\omega_c/\omega_p \simeq 1 - 3 \times 10^{-3}$. These values indicate that any modifications to the dispersion relations due to the imposed B-field are negligible under the current simulation conditions.

## III. SIMULATION RESULTS

A comparison of the EPW potential between unmagnetized (0 T) and magnetized (30 T) cases is shown in Fig. 1. Panels 1(a) and 1(b) display the real component of the EPW potential at 10.8 ps. The EPW

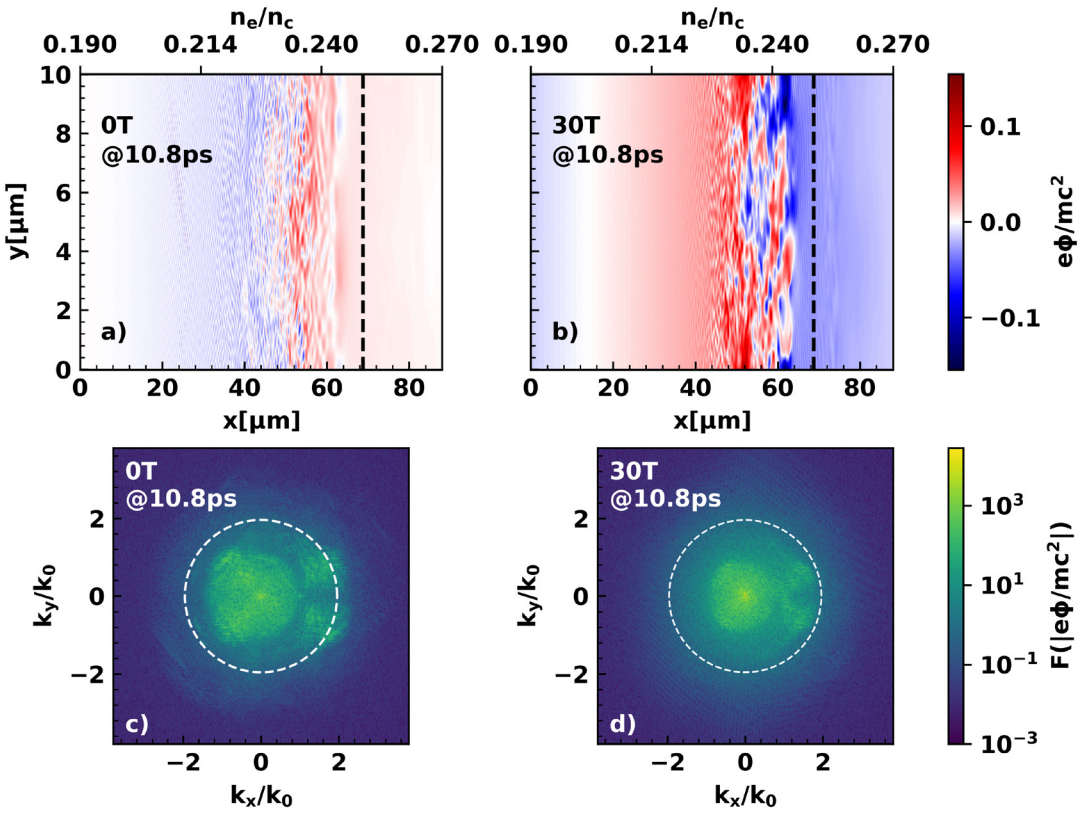


**FIG. 1.** Real component of the electron plasma wave potential in real (a) and (b) and Fourier space (c) and (d) at $\sim$ 10.8 ps, in the unmagnetized (0 T, left) and magnetized case (30 T, right). The black dashed line in (a) and (b) represents the position of $n_c/4$, while the white dashed circle in (c) and (d) represents $k_{EPW}\lambda_{De} \simeq 0.3$.

potential exhibits turbulent behavior, attributed to both LDI and LW collapse. The highest potential is localized near the quarter critical density $n_c/4$ (black dashed line) at $x_c \simeq 68\,\mu$m. This spatial structure is driven by the temporal growth of SRS and TPD instabilities near quarter critical, leading to absolute SRS/TPD. During the simulation, these instabilities propagate toward lower densities [Fig. 1(a)] and undergo spatial amplification (convective SRS/TPD).[58] When a magnetic field is introduced [Fig. 1(b)], the backward propagation of EPWs is restricted closer to $n_c/4$, and the EPW potential at lower densities is significantly reduced. For the 30 T case, the strongest EPWs are confined between 40 and 65 $\mu$m, compared to the broader $20-65$ $\mu$m region observed without magnetization.

Figures 1(c) and 1(d) present the EPW potentials in Fourier space. These plots reveal the characteristic "lobed" structures of TPD growth[17] at $[k_x, k_y] \simeq [-0.8, \pm 0.8]$ (appearing only in the 0 T case) and at $[k_x, k_y] \simeq [1.8, \pm 0.8]$ (visible in both 0 and 30 T cases). Turbulence from LDI cascades[22] and LW collapse[23] results in homogeneous wave emission, with random EPW modes distributed in a circle centered at $[k_x, k_y] \simeq [0, 0]$. Backscattered SRS-generated EPWs are weak in the 0 T case, evident only near $[k_x, k_y] \simeq [1, 0]$; these features are likely obscured by turbulent wave emission from TPD due to a comparatively weaker SRS signal. The boundary of turbulent EPW emission is demarcated by a white dashed circle in plots (corresponding to $k_{EPW}\lambda_{De} \gtrsim 0.3$, where $\lambda_{De}$ is the Debye length); beyond this, strong Landau damping occurs, causing a rapid decrease in EPW amplitude. The 30 T magnetic field reduces the radius of the homogeneous emission circle, and modes outside $[k_x, k_y] \simeq [\pm 0.5, \pm 0.5]$ are weaker, highlighting a suppression of EPW activity relative to the unmagnetized scenario.

The results in the magnetized case can be interpreted by examining the electron and EPW dynamics at lower densities, specifically in the region around 25–50 $\mu$m in Fig. 1(b). Here, EPWs exhibit higher wavenumbers and therefore lower phase velocities. The gyration motion of electrons under the influence of the applied B-field causes them to be trapped near EPWs between $\sim 25$ $\mu$m and $n_c/4$, increasing the probability for resonance between the electron longitudinal velocity component and the EPW phase velocity.[46] As a result, more electrons are accelerated to higher energies by acquiring energy from the EPWs, leading to more HEs. In turn, this increased HE population leads to stronger EPW Landau damping in the plasma. The probability of resonance is particularly high for EPW modes with large wavenumber $k$ (and thus lower $v_{ph}$), which are found at densities below $n_c/4$, in the $\sim 25-50$ $\mu$m region. These resonant electrons typically lie in the mid-energy range ($\varepsilon \simeq 20$–35 keV), where their thermal velocity matches $v_{ph} \simeq 3$–$5\,v_{Te}$. The net effect is a reduction in EPW mode amplitude in Fourier space [Fig. 1(d)] and the suppression of EPWs in real space within 25–50 $\mu$m, as highlighted in Fig. 1(b). Further quantification is given in Fig. 2(a), which compares angle-averaged Landau damping as a function of $k\lambda_{De}$ for 0 and 30 T cases. Above $k\lambda_{De} \simeq 0.12$, Landau damping in the 30 T case consistently exceeds that in the 0 T case, explaining the diminished EPW presence seen in Fig. 1(d) when compared to Fig. 1(c). This mechanism, where electron gyration enhances HE production and thus Landau damping, is also supported by previous work,[59] which predicts that a sufficiently strong magnetic field can increase Landau damping provided that $\gamma \equiv t_t/t_c$ approaches 0.1–1 ($t_t$: trapping time; $t_c \sim \omega_c^{-1}$: cyclotron time). In our simulations, with $t_t \sim 0.1$–1 ps and B-fields between 15 and 45 T, we find $\gamma \simeq 10^{-2} - 10^{0}$, corroborating the observed enhancement of EPW Landau damping due to the applied B-field.

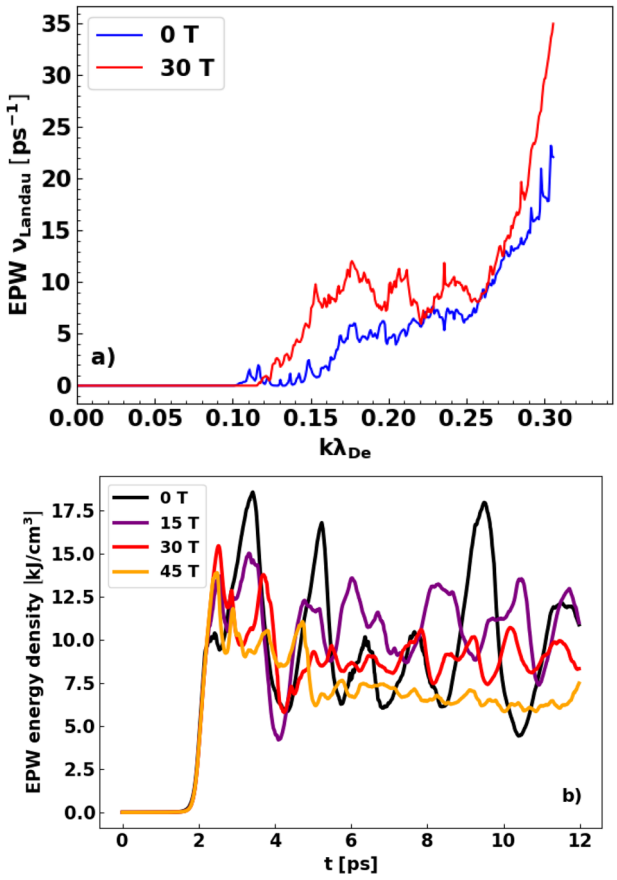


FIG. 2. (a) Angular average of the EPW Landau damping from the 2D simulations, as a function of $k\lambda_{De}$, both for the unmagnetized (blue) and 30 T (red) case. (b) Spatially-averaged EPW energy density as a function of time, for different applied magnetic fields.

Expanding on the previous analysis, Fig. 2(b) shows the spatially averaged EPW energy density as a function of time, including various B-field strengths (from 0 T to 45 T). At early times (from 0 to $\sim 2.5$ ps), the instabilities grow exponentially over time. Around $\sim 2.5$ ps, effects from LDI, cavitation, and HE generation begin to appear, driving saturation of SRS and TPD. The EPW energy density subsequently stabilizes, reaching quasi-stationary levels by $\sim 4.5$ ps, which persist until the end of the simulation. In the absence of a magnetic field, strong energy fluctuations occur due to laser pump depletion; these oscillations diminish as the B-field strength increases. The average EPW energy at 15 T is similar to the 0 T case, from which it can be deduced that the magnetic field strengths that begin to significantly modify LPIs are in the range of $\sim 10^1$ T. Additionally, the quasi-stationary EPW energy density decreases with higher B-field, dropping from $\sim 11$ kJ/cm$^3$ at 15 T to $\sim 6$–$7$ kJ/cm$^3$ at 45 T. This trend highlights the suppressive impact of the magnetic field on EPW energy, consistent with enhanced Landau damping and reduced instability saturation observed in magnetized scenarios.[60,61]

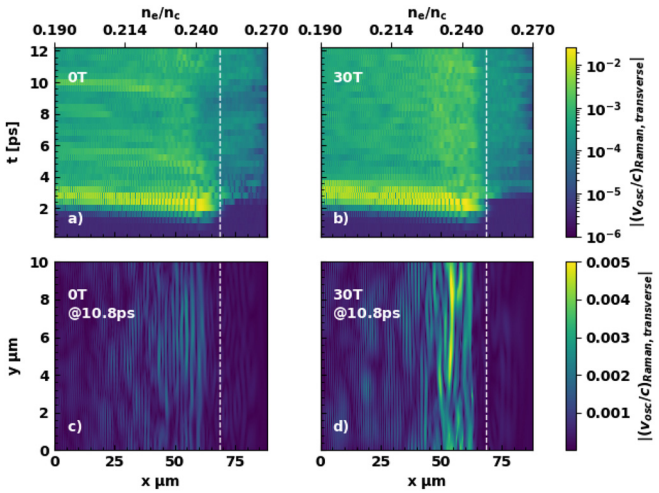


**FIG. 3.** (a) and (b) y-averaged absolute value of the Raman electric field as a function of the x coordinate and time. (c) and (d) Longitudinal Raman electric field (in units of $v_{osc}/c$) as a function of 2D space at the same time as Fig. 1, 10.8 ps. The white dashed line is the $n_c/4$ position.

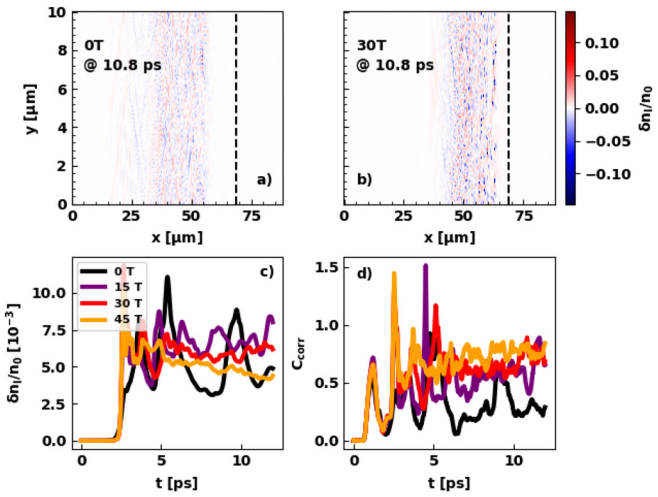


**FIG. 4.** 2D map of the low-frequency electron density perturbation normalized to the envelope density $\delta n_l/n_0$, indicating IAW activity, both in the (a) unmagnetized and (b) magnetized case at 10.8 ps. The dashed black line is the $n_c/4$ location. (c) Root mean square spatial averaged $\delta n_{elf}/n_0$ signal and (d) caviton correlator parameter $C_{corr}$ as a function of applied B-field. $T_e = 3$ keV and $L_n = 250$ $\mu$m in every plot.

Having examined EPWs, we next evaluate the effects of magnetization on other plasma waves, specifically Raman-scattered light and IAWs. Figures 3(a) and 3(b) show the spatially averaged Raman scattered light field (i.e., the transverse component of the response field $\mathbf{E_l}$ in units of $v_{osc}/c$) as a function of laser propagation direction and time. Initially (up to $t \sim 2$ ps), Raman light grows exponentially and propagates toward regions of lower density. This growth diminishes around $t \simeq 3$ ps, coinciding with the onset of Langmuir turbulence from LDI, LW collapse, and increased hot electron generation. Afterward, the Raman light field is greatly weakened but remains observable: for $n_e > n_c/4$, fields are $v_{osc}/c \sim 5 \times 10^{-4}$, while for $n_e < n_c/4$, they range from 4 to $5 \times 10^{-3}$. Below $n_c/4$, regions of elevated Raman activity emerge in both the 0 and 30 T cases, similar to the EPW potential distributions in Fig. 1. This is visible in the real-space plots at 10.8 ps [Figs. 3(c) and 3(d)], which reveal high-activity regions overlapping with those found for EPWs. While backward-propagating Raman waves obscure the exact boundaries of these regions, the most notable feature is the concentration of strong Raman fields in the magnetized (30 T) case, localized within 40–65 $\mu$m, similar to the corresponding EPW-dominated region in Fig. 1(b). These areas result from SRS acting where electron density fluctuations (or EPWs) maximize coupling to the incident laser, thus driving stronger backscattered Raman waves. Notably, the amplitude of the Raman light field is an order of magnitude lower than the EPW field. By analyzing Figs. 3(c) and 3(d), we estimate the average Raman reflectivity at the left boundary (far from $n_c/4$) to be about 1%–2% of the total laser energy. In contrast, laser transmissivities for 0 and 30 T cases (see Sec. IV) are $\sim$ 45%–55%, inferring that TPD dominates energy dissipation over SRS during the simulation, where absolute TPD is bound to grow. This is consistent with expectations for p-polarized laser light (where TPD is active), whereas s-polarization would suppress TPD and favor SRS.[62–64] This dominance of TPD over SRS is limited to the region near $n_c/4$. As specified in Sec. II, the simulations do not take into account the important role that convective SRS plays in absorbing laser energy even before the drive light reaches quarter critical, which could be an interesting point for future research.

Finally, we assess the behavior of IAWs and low-frequency density perturbations. Figures 4(a) and 4(b) display the normalized low-frequency electron density perturbation ($\delta n_l/n_0$), a diagnostic for IAW and LDI activity. These waves are spatially confined to regions similar to the EPW potentials shown previously in Fig. 1. In Fig. 4(c), the time evolution of the spatially averaged $\delta n_l/n_0$ is shown for different B-field strengths. The evolution of $\delta n_l/n_0$ parallels that of the EPW energy density, with rapid growth beginning around $t \sim 2.5$ ps—consistent with the onset of LDI and associated saturation seen in Fig. 2(b). As the system reaches quasi-stationary conditions at $t \simeq 5$ ps, the mean IAW signal is slightly higher in simulations with applied (15, 30, and 45 T) magnetic fields compared to the unmagnetized (0 T) case. However, as B-field strength exceeds 15 T, the IAW signal declines, with the 15, 30, and 45 T curves closely grouped. Overall, these results indicate that in magnetized simulations ($B > 0$ T), IAWs are more spatially confined, and the low-frequency density perturbations are concentrated where EPWs remain active. While IAW amplitudes are enhanced locally, stronger B-fields reduce their overall activity region, leading to a net decrease in the mean signal for higher field strengths.

This enhancement of low-frequency electron density perturbations signals an increase in Langmuir turbulence activity, specifically LW collapse, within the simulation domain. Any LPI generating an EPW as a daughter wave can launch subsequent LDI, including secondary EPWs from LDI itself if their matching conditions are met. This process creates a "cascade" of LDIs, in which the EPW wavenumber $\mathbf{k_{EPW}}$ decreases at each decay step by a factor $\Delta k \equiv (2/3)[c_s/(v_{Te}\lambda_{De})]$.[22] As the cascade proceeds, low-wavenumber EPW modes (corresponding to long-wavelength density perturbations) accumulate near $n_c/4$. When these EPWs reach sufficient amplitude, they drive the formation of pronounced density

depressions ("cavitons"), which subsequently collapse on a timescale $t_{collapse}$, generating strong Langmuir turbulence[23] that detunes TPD-generated EPWs.[63] A quantitative measure of LW collapse and caviton formation is provided by the "caviton correlator," whose temporal evolution for various B-field strengths is shown in Fig. 4(d). This diagnostic, defined in Refs. 65 and 66, captures the prevalence and dynamic evolution of cavitons, offering a direct indicator of Langmuir turbulence in the system.

$$C_{corr} \equiv \frac{\langle -\delta n_l |E_{EPW}|^2 \rangle}{\left( \langle \delta n_l^2 \rangle^{1/2} \langle |E_{EPW}|^2 \rangle \right)}. \quad (2)$$

The caviton correlator, $C_{corr}$, quantifies the spatial correlation between IAW-driven density depressions and EPW field peaks. A value of $C_{corr} \gtrsim 0.5$ indicates a strong correlation and signifies vigorous Langmuir wave (LW) collapse activity in the plasma.[66] As shown in Fig. 4(d), after the system reaches quasi-stationary conditions, $C_{corr}$ remains relatively weak in the unmagnetized (0 T) case, at approximately 0.25, but increases noticeably with stronger magnetic fields. This trend is consistent with the observed rise in the number of IAW density depressions (i.e., cavitons) evident in the 30 T case [Fig. 4(b)] compared to the 0 T scenario [Fig. 4(a)]. This enhancement is likely due to the preferential damping of high-$k$ EPW modes by the magnetic field, allowing low-$k$ (long-wavelength) EPWs to dominate and form dense caviton structures more readily. Thus, stronger B-fields promote both the occurrence of cavitons and the manifestation of pronounced LW collapse activity in the system.

## IV. TRANSMISSIVITY

Figure 5(a) shows the time evolution of the laser transmissivity for plasma parameters $T_e = 3$ keV and $L_n = 250\,\mu$m, comparing unmagnetized (0 T) and magnetized (30 T) cases. Initially, the laser transmits fully (100%), but transmissivity declines as LPIs, turbulence, and hot electron generation develop, until reaching quasi-stationary conditions. Notably, the 30 T case maintains a consistently higher laser transmissivity, approximately 8%–10% greater than the 0 T case, improving from about 38%–40% to 45%–50%. This enhanced transmissivity is primarily attributed to the suppression of EPW activity in the magnetized plasma, which reduces pump depletion.

To disentangle the contributions of the two primary parametric instabilities, SRS and TPD, to the observed reduction in laser transmissivity, we performed a series of simulations in which only SRS or only TPD was allowed to operate, both with and without saturation effects from LDI and turbulence, and in unmagnetized and magnetized conditions. This allowed us to assess the individual and combined impacts of the magnetic field on each instability. It should be noted that isolating individual instabilities in simulation is not physically rigorous, as in realistic plasma environments, competition and nonlinear interactions between instabilities naturally drive the system toward quasi-stationary conditions. Nonetheless, this approach provides valuable insight into how an applied magnetic field affects the dynamics of each instability in isolation.

Figure 5(b) explores laser transmissivity in simulations where only SRS is active, under various conditions. Red and blue lines indicate simulations with and without turbulence, respectively, reflecting the inclusion or exclusion of IAWs (which permit LDI and LW collapse). Solid and dashed lines distinguish magnetized (30 T) and

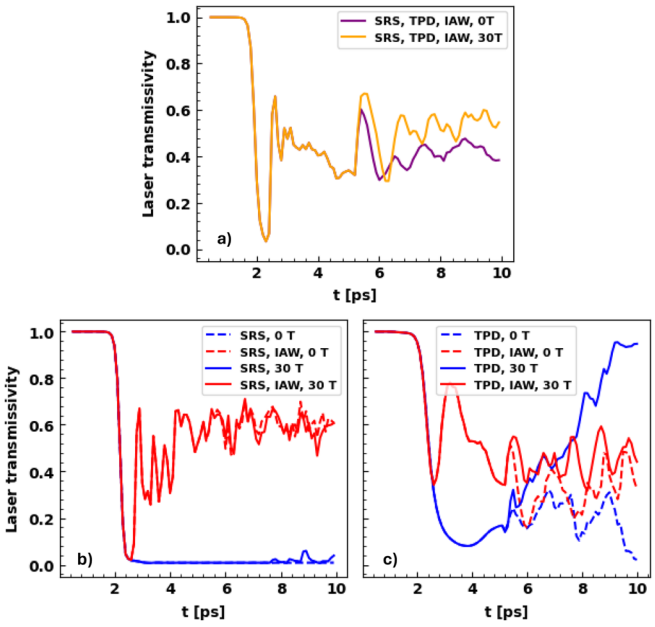


**FIG. 5.** Laser transmissivity as a function of time for (a) the complete system with SRS, TPD and LDI/LW collapse for 0 T (purple) and 30 T (orange); (b) SRS only and (c) TPD only, in the unmagnetized (dashed) and magnetized (full line) 30 T case, and in the absence (blue) or presence (red) of IAWs and turbulence, be it from LDI or LW collapse. The simulations have parameters $T_e = 3$ keV and $L_n = 250\,\mu$m.

unmagnetized cases (0 T). When IAWs are absent, neither pump depletion nor hot electron generation suffices to saturate SRS; instead, the instability grows unchecked, rapidly absorbing all laser energy, and the transmissivity drops to nearly zero after $\sim 2.5$ ps. The introduction of a magnetic field has no appreciable effect on this outcome, indicating that neither ballistic nor gyrating electrons substantially affect SRS activity under these conditions. This behavior is consistent with systems dominated by backscattered SRS,[13] wherein EPWs generated parallel to laser propagation do not provide significant resonance with electrons regardless of their trajectories. Adding turbulence via IAWs introduces a strong saturation mechanism for SRS, dramatically increasing laser transmissivity to nearly 60%. However, in this regime, the presence or absence of an applied B-field does not further alter transmissivity outcomes. Although the EPW potential becomes more turbulent (reflected by a full circle of EPW modes in Fourier space) when IAWs are present, its amplitude is roughly four times lower compared to cases with pure SRS alone. Overall, these results demonstrate that, when SRS dominates, hot electron generation and energy depletion are largely independent of both turbulence and the electron trajectories induced by the applied magnetic field.

In contrast, Fig. 5(c) examines simulations where only TPD is active, structured analogously to the SRS-only results, i.e., with and without IAWs (turbulence), and with or without a magnetic field. In the absence of IAWs and without a B-field, laser transmissivity reaches a quasi-stationary value near 20%. When a 30 T B-field is applied (still without IAWs), there is an initial decrease in transmissivity similar to the 0 T scenario up to $t \simeq 5$ ps. However, starting from 4 ps, laser transmissivity rebounds and nearly restores to 100%—indicating an

almost complete suppression of TPD in the magnetized case. This behavior results from the lack of saturation mechanisms such as LDI: with no decay process to breakup high-$k$ EPW modes, the combination of low TPD phase velocities and enhanced electron gyration enables more electrons to resonate with the EPWs, thereby strongly increasing Landau damping and suppressing the instability. Introducing turbulence via IAWs mitigates this effect. In these cases, high-$k$, low-$v_{ph}$ EPW modes are promptly removed by LDI, enabling effective absorption even in the presence of a strong B-field. Quantitatively, the difference in quasi-stationary laser transmissivity is approximately 10%, mirroring the trend seen in the combined SRS+TPD results of Fig. 5(a).

Taken together, the results in Fig. 5 demonstrate that an external B-field substantially suppresses TPD activity, while SRS remains largely unaffected. This distinction persists regardless of the development of turbulence from LDI and Langmuir wave collapse (introduced via the presence or absence of IAWs). It should be emphasized that, under the conditions explored here, namely, a p-polarized laser drive, TPD is the dominant instability near $n_c/4$; as such, the simulation outcomes primarily reflect B-field effects on TPD rather than SRS. Exploring s-polarized scenarios would be a valuable extension for future work, as these would emphasize SRS and allow for a systematic study of its magnetic field sensitivity.[60,61]

## V. HOT ELECTRON GENERATION

Next, we examine hot electron (HE) generation by comparing results from unmagnetized and magnetized simulations. Figures 6(a) and 6(b) illustrate the velocity distribution function (VDF), in units of $(m/s)^{-2}$, for the 0 and 30 T cases, respectively, in 2D velocity space. In both cases, the majority of plasma electrons follow a Maxwell-Boltzmann distribution in velocity space, reflecting a thermalized bulk population, while HEs belong to the high-energy tail departing from this distribution. In the unmagnetized case [Fig. 6(a)], HEs exhibit a strongly preferential emission in the forward (laser propagation) direction and tend to propagate toward higher-density regions. In contrast, backward-directed HE generation is substantially weaker.

In contrast, the magnetized case (30 T) depicted in Fig. 6(b) reveals a markedly different velocity distribution for the hot electrons. Here, the VDF shows that HE emission becomes much more isotropic, forming a "cloud" of energetic electrons distributed around the Maxwell–Boltzmann core, rather than being preferentially beamed forward as in the 0 T scenario. This isotropic distribution arises when electrons undergo rapid gyromotion due to the applied magnetic field, effectively randomizing their emission directions relative to the laser propagation axis. Despite this change in angular distribution, the maximum electron speeds in both unmagnetized and magnetized cases reach $|v|/c \simeq 0.55$–$0.6$, corresponding to energies of approximately 100–130 keV. Thus, while the B-field alters the directionality of HE emission, maximum electron energies remain similar across both cases.

Figure 6(c) displays the angularly averaged VDF for applied B-field strengths of 0, 15, 30, and 45 T. Above $v/c \simeq 0.42$ (corresponding to $\sim 52$ keV), the HE tail grows substantially with increasing magnetic field: relative to the unmagnetized case, the HE population increases by a factor of 2 at 15 T and nearly 8 at 45 T, corroborating findings from Ref. 48 that magnetic fields enhance HE generation. Additionally, the magnetized simulations exhibit a 25% − 50% rise in the number of electrons at the distribution's tail ($v/c \simeq 0.25$–$0.325$, or 17–30 keV) compared to 0 T. In the absence of a magnetic field, HEs

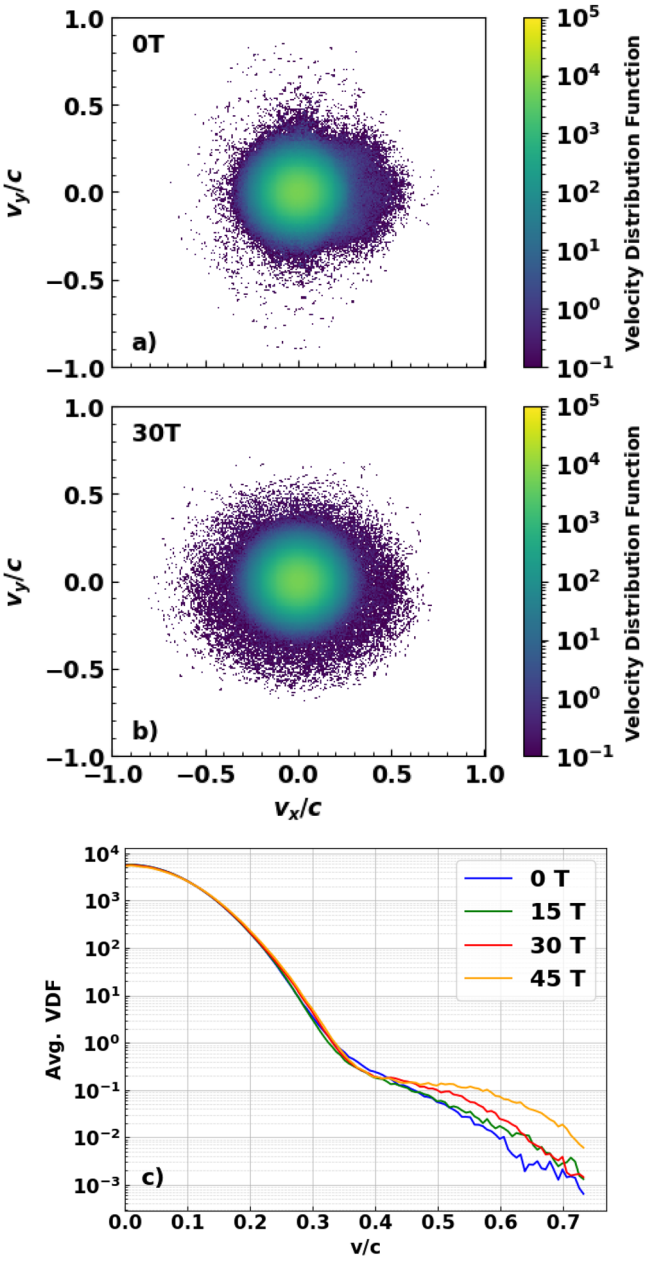


**FIG. 6.** Time average of the velocity distribution function (VDF) in 2D velocity space in (a) the unmagnetized and (b) the magnetized (30 T) case. (c) Angular average of the VDF for 0, 15, 30, and 45 T. Plasma parameters are $T_e = 3$ keV and $L_n = 250$ $\mu$m in all plots.

are primarily generated from the tail of the Maxwellian distribution and gain further energy via staged interactions with the LPI front at $n_c/4$, as previously described in Ref. 67. However, in the presence of a strong enough B-field, electron gyromotion enables multiple crossings of the LPI front, increasing the resonance probability both for mid-energy (17–30 keV) electrons and for HEs ($\gtrsim 50$ keV). This enhanced resonance boosts the HE population, which in turn raises the EPW

Landau damping rate, compounding the stronger spatial confinement of EPW activity observed in Sec. III.

To further elucidate electron gyration and energy gain mechanisms, we analyze representative particle trajectories from the 30 T, 3 keV, 250 $\mu$m simulation. Figures 7(a) and 7(b) illustrate two particle paths in real space, a thermal electron and a HE, with their respective start points (black dots) and endpoints (red dots) marked. Colors along each trajectory indicate instantaneous electron energy. Both electrons start with gyromotion defined by their Larmor radii, which scales with energy. The thermal electron traces a relatively stable orbit ($\rho_L \sim 5$–$6\,\mu$m), consistent with its Maxwell–Boltzmann energy (2–3 keV). The HE, on the other hand, begins with a much larger orbit ($\rho_L \sim 15$–$16\,\mu$m, 20–22 keV) and undergoes a dramatic increase to $\rho_L \sim 30$–$31\,\mu$m (90 keV) after interacting with strong EPW fields near $[x, y] \simeq [50, 70]\,\mu$m. The HE momentarily reaches 160 keV before stabilizing near 90 keV due to ongoing energy exchange with the EPW region close to $n_c/4$. The thermal electron's path is heavily perturbed by turbulent EPW low-wavenumber modes, resulting in a chaotic trajectory. Conversely, the HE trajectory remains ordered; its high energy allows it to stay resonant with the EPW field and avoid significant disruption by low-frequency turbulence. Notably, the HE also displays a guiding center drift by electric field effects that is proportional to $(\mathbf{E} \times \mathbf{B})/B^2$, a feature absent in the thermal electron's more turbulent trajectory.

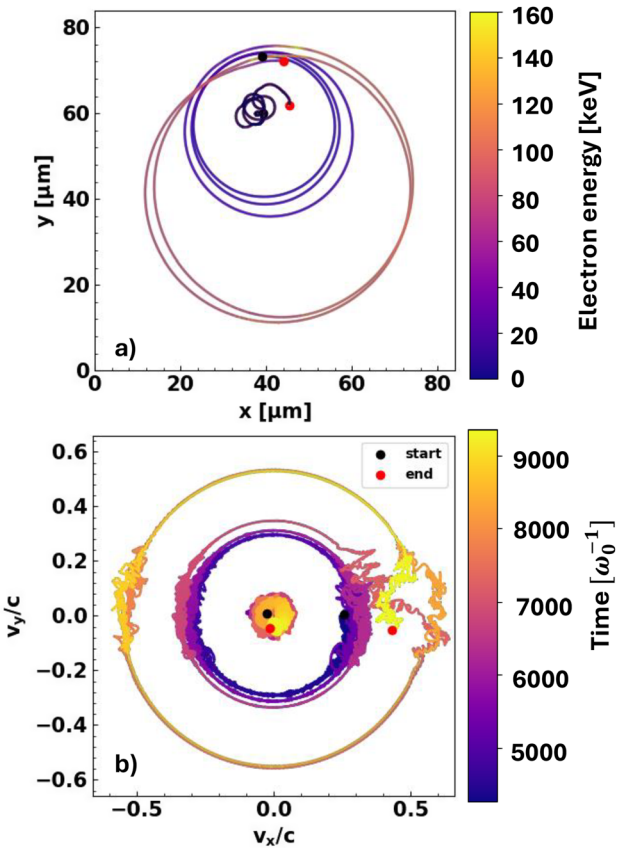


**FIG. 7.** (a) Particle trajectories in 2D real space and (b) velocity space of a thermal plasma electron and a HE. Both plots are in the magnetized, 30 T case. The simulation plasma temperature is $T_e = 3$ keV, the density scale length is $L_n = 250\,\mu$m.

Figure 7(b) presents the same thermal and hot electron (HE) trajectories as Fig. 7(a), now mapped in 2D velocity space. Like the frameworks in Winjum *et al.*[46] and Li *et al.*,[48] this plot uses line color to represent time (normalized to the laser frequency $\omega_0$) and marks trajectory start/end points as before. The thermal electron's path confirms it acquires little additional energy; its velocity distribution remains tightly grouped and consistent with Maxwellian thermal motion. In contrast, the HE exhibits intermittent, strong oscillations in velocity space, most notably when its longitudinal velocity component grows larger than the transverse one. In these intervals, the electron becomes "trapped" by EPWs at the LPI front, gaining energy through successive bounces. Once its transverse velocity reaches the detrapping value, $v_y = cE_x/B_0$, the electron escapes, having increased its energy and Larmor radius. This bouncing and detrapping mechanism contributes to energy growth for both forward and backward-directed electrons, in agreement with prior studies of TPD-driven acceleration.[48] Compared to previous work,[46,48] we observe a narrower range of transverse velocities where these bounces occur, most likely due to enhanced Langmuir turbulence and stronger EPW mode saturation from LDI and LW collapse, which were not included in these previous works. As a result, energy growth is gradual, accumulating over several orbits, rather than manifesting in a single, sudden burst. Rare events of strong EPW-electron resonance, such as the one at $t\omega_0 \simeq 6500$, produce multi-stage acceleration and larger Larmor radii,[67] echoing known mechanisms in unmagnetized plasmas. Importantly, the increased confinement provided by the applied B-field allows electrons to spend more time near the LPI region around $n_c/4$, increasing the likelihood of these rare, energy-boosting encounters.

Figure 8(a) presents the normalized HE energy flux at the simulation right boundary (high-density side) under quasi-stationary conditions for different B-field strengths. In the unmagnetized scenario, the fraction of HEs leaving the simulation right boundary is $f_{HE} \simeq 14.7\%$, with an average HE temperature of $T_{HE} \simeq 23$ keV. When a strong magnetic field is applied, the HE flux is reduced by up to a factor of 5 in the 45 T case with $f_{HE} \simeq 2.8\%$, while the average HE temperature reaches $T_{HE} \simeq 53$ keV, which is nearly 56% higher than for the unmagnetized case. These findings complement the demonstration of enhanced HE production and heating found in Fig. 6(c) and Ref. 48. Importantly, Fig. 8(a) confirms that, while a magnetic field increases HE production [Fig. 6(c)], it also strongly confines these HEs near the $n_c/4$ region. Effectively, fewer HEs can penetrate to higher densities, thus mitigating the risk of preheat in an ICF scenario despite higher average HE temperatures.

While we primarily focused before on simulations without and with a 30 T B-field to highlight the contrast between magnetized and unmagnetized regimes (at $T_e = 3$ keV and $L_n = 250\,\mu$m), these cases form part of a broader parameter scan designed to map magnetized LPI behavior near quarter-critical density. Figure 8(b) summarizes the scan results, plotting the HE fraction as a function of magnetic field strength for varied plasma conditions. The scan encompasses 20 simulations: $T_e = 1, 3, 4$ keV; $L_n = 150, 200, 250\,\mu$m; and B-fields of 0, 15, 30, and 45 T. The trend is clear: stronger B-fields consistently reduce the HE flux at the simulation right boundary. In the most energetic configuration (4 keV, 250 $\mu$m), the fraction of HE leaving the right boundary drops sharply, from $f_{HE} \sim 24.5\%$ at 0 T to $\sim 5\%$ at 45 T.

Examining the HE fractions for constant $L_n$ but varying electron temperatures $T_e$, we observe that raising $T_e$ consistently increases this

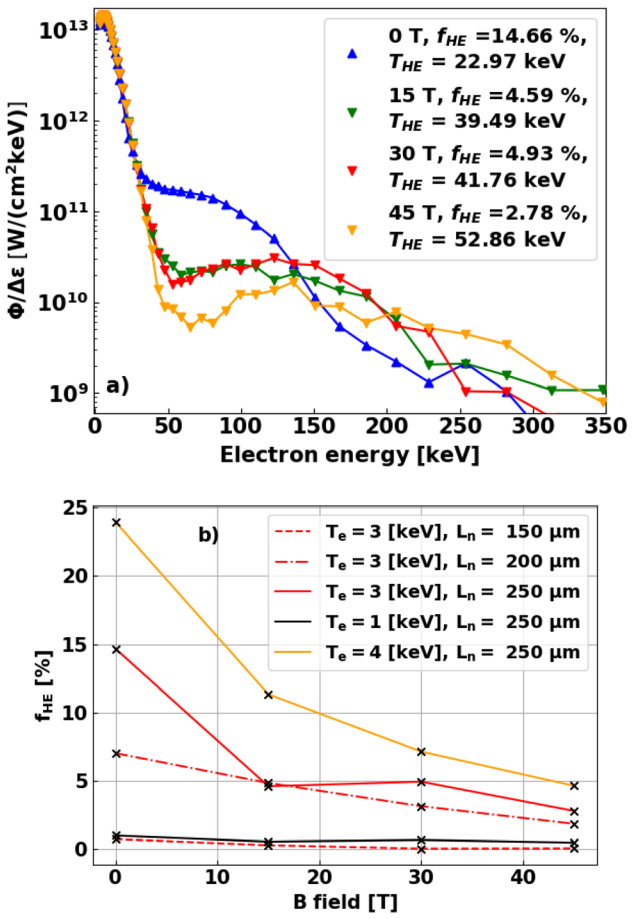


**FIG. 8.** (a) Time-averaged normalized electron energy flux at the simulation right boundary (high-density side) as a function of electron energy, for the magnetized and unmagnetized cases. Plasma parameters are $T_e = 3$ keV and $L_n = 250$ $\mu$m. (b) Fraction of HEs leaving the simulation right boundary as a function of applied B-field strength. Plasma parameters are varied, with $T_e = 1, 3, 4$ keV and $L_n = 150, 200, 250$ $\mu$m.

fraction, for both 0 T and magnetized cases. This trend aligns with the expectation that EPW collisional damping, $\nu_{EPW} = \nu_{ei}/2 \propto T_e^{-3/2}$, becomes weaker as $T_e$ increases. In cooler plasmas ($T_e = 1$ keV), stronger collisional damping severely suppresses HE production: the calculated EPW damping rates are $\nu_{coll}^{EPW} \simeq 0.78$ ps$^{-1}$ for $T_e = 3$ keV, $L_n = 250$ $\mu$m, rising to 3.46 ps$^{-1}$ for $T_e = 1$ keV.

Turning to the density scale length parameter ($L_n$) scan at fixed electron temperature ($T_e = 3$ keV), we find that the HE fraction is strongly influenced by $L_n$. For the largest scale length (250 $\mu$m), $f_{HE}$ declines sharply from about 15% to 4% as the applied B-field increases from 0 T to 15 T. In contrast, reducing $L_n$ mitigates this drop, as seen in the 200 and 150 $\mu$m curves. Physically, a shorter density scale length limits the region where LPIs form, which reduces electron resonance with instabilities and lowers the HE fraction. This effect is seen in both magnetized and unmagnetized cases.[68,69] Therefore, reducing $L_n$ consistently decreases HE production and diminishes the influence of the magnetic field.

## VI. CONCLUSIONS

This work presents a comprehensive analysis of laser–plasma instabilities near quarter-critical density ($n_c/4$), including SRS, TPD, LDI, and LW collapse, both in the absence and presence of applied magnetic fields. Using 2D LPSE simulations, we mapped spatial fields of EPWs, Raman scattering, and IAWs. Application of a magnetic field confines EPW activity to a narrower region near $n_c/4$ and enhances Landau damping, as confirmed by Fourier-space diagnostics. The Raman and IAW fields similarly exhibit signatures of increased EPW localization. Additionally, cavitation and LW collapse activity are observed to intensify with increasing magnetic field strength.

To determine the influence of each instability and turbulence with the applied magnetic field, we conducted a series of simulations that selectively enabled only SRS, only TPD, or both, with IAWs either included or excluded, and with either 0 T or 30 T. The SRS signal is strongly affected by the inclusion of IAWs, which act as a saturation mechanism, but shows little sensitivity to the magnetic field, noting that the use of p-polarized light in these simulations preferentially energizes TPD over SRS. In TPD-only runs, near-total absorption of EPWs occurs when IAWs are excluded, while including IAWs introduces plasma turbulence that stabilizes both TPD growth and the effect of gyrating electrons by the applied magnetic field. Finally, when both instabilities and IAWs are present, adding a 30 T magnetic field increases laser transmissivity by roughly 10%, due to the increased damping of TPD.

Velocity distribution function (VDF) analysis reveals that, in the presence of a magnetic field, hot electrons are emitted isotropically rather than predominantly in the forward direction. This isotropy arises as electron trajectories transition from a ballistic to a gyrating motion under the influence of the applied B-field. The overall HE population grows with increasing B-field, which in turn enhances EPW Landau damping and confines EPW activity closer to $n_c/4$. Particle trajectory analysis confirms that gyrating electrons repeatedly traverse the LPI region near quarter-critical density, enabling multiple opportunities for energy gain and HE generation. On the other hand, stronger magnetic fields also restrict the HE flux toward higher densities. Therefore, while magnetization increases the total number of HEs and the average temperature of HEs streaming toward higher densities, more electrons remain confined near $n_c/4$ overall, minimizing preheat risk in ICF targets.

Finally, we carried out a scaling analysis of the HE fraction reaching the high-density side of the simulation across a range of plasma conditions, varying electron temperature ($T_e$), density scale length ($L_n$), and magnetic field strength (15–45 T). An increase in plasma temperature was found to raise $f_{HE}$ in both unmagnetized and magnetized plasmas. By contrast, reducing the density scale length not only decreased the overall production of HEs, as expected, but also softened the drop in $f_{HE}$ observed when transitioning from unmagnetized to magnetized conditions.

These findings advance the understanding of magnetized laser–plasma interactions and suggest that hot electron preheat in ICF can be reduced by applied or self-generated magnetic fields persisting around quarter-critical density. Magnetic fields can also enhance laser heating in plasmas (such as in MagLIF) by increasing hot electron generation from LPIs and simultaneously confining these electrons within the heated region. Additionally, the radiation from gyrating electrons (at the cyclotron frequency) presents opportunities for THz wave generation. Future work should investigate more complex geometries between the laser and magnetic fields to further quantify the impact of

magnetic confinement on LPI-driven hot electron generation and transport, with broader implications for optimizing fusion energy and advancing plasma diagnostics.

## ACKNOWLEDGMENTS

This work was supported by the U.S. National Nuclear Security Administration (NNSA) and National Laser Users' Facility under Award No. DE-NA0003940 and by the U.S. Department of Energy—NNSA, under Grant No. DE-NA0004199. Simulations were performed on the UCSD Expanse SDSC cluster, under Project No. PHY240048 and a Discover allocation. This work has also been carried out within the framework of the EUROfusion consortium, funded by the European Union via the Euratom Research and Training Program (Grant Agreement No. 101052200–EUROfusion). The involved teams have operated within the framework of the Enabling Research Project AWP24-ENR-IFE.02.CEA-01. This research was funded, in part, by the French Agence Nationale de la Recherche (ANR), Project No. ANR-22-CE30-0044. This work has been supported by Research Grant No. PID2022-137632OB-I00 from the Spanish Ministry of Science and Innovation.

## AUTHOR DECLARATIONS

### Conflict of Interest

The authors have no conflicts to disclose.

### Author Contributions

**E. Rovere:** Conceptualization (lead); Data curation (lead); Formal analysis (lead); Investigation (lead); Methodology (equal); Resources (lead); Software (equal); Visualization (lead); Writing - original draft (lead); Writing - review & editing (equal). **R. K. Follett:** Data curation (equal); Investigation (equal); Methodology (equal); Software (lead); Writing - review & editing (equal). **F. S. Tsung:** Investigation (equal); Validation (equal); Writing - review & editing (equal). **B. J. Winjum:** Investigation (supporting); Validation (equal). **J. J. Santos:** Investigation (supporting); Writing - review & editing (supporting). **G. Pérez-Callejo:** Investigation (supporting); Writing - review & editing (equal). **R. Florido:** Investigation (supporting); Writing - review & editing (supporting). **A. Bordón-Sanchez:** Investigation (supporting); Writing - review & editing (supporting). **M. Caetano de Sousa:** Investigation (supporting); Writing - review & editing (supporting). **M. A. Gigosos:** Writing - review & editing (supporting). **F. N. Beg:** Investigation (supporting); Supervision (supporting); Writing - review & editing (equal). **M. Bailly-Grandvaux:** Conceptualization (equal); Data curation (equal); Funding acquisition (lead); Investigation (equal); Methodology (equal); Project administration (lead); Supervision (lead); Writing - review & editing (equal).

## DATA AVAILABILITY

The data that support the findings of this study are available from the corresponding author upon reasonable request.

## REFERENCES

[1]J. F. Drake, P. K. Kaw, Y. C. Lee, G. Schmid, C. S. Liu, and M. N. Rosenbluth, "Parametric instabilities of electromagnetic waves in plasmas," Phys. Fluids **17**, 778 (1974).
[2]R. White, P. Kaw, D. Pesme, M. N. Rosenbluth, G. Laval, R. Huff, and R. Varma, "Absolute parametric instabilities in inhomogeneous plasmas," Nucl. Fusion **14**, 45 (1974).
[3]J. P. Palastro, J. G. Shaw, R. K. Follett, A. Colaïtis, D. Turnbull, A. V. Maximov, V. N. Goncharov, and D. H. Froula, "Resonance absorption of a broadband laser pulse," Phys. Plasmas **25**, 123104 (2018).
[4]P. Kaw, G. Schmidt, and T. Wilcox, "Filamentation and trapping of electromagnetic radiation in plasmas," Phys. Fluids **16**, 1522 (1973).
[5]A. B. Langdon and B. F. Lasinski, "Filamentation and Subsequent Decay of Laser Light in Plasmas," Phys. Rev. Lett. **34**, 934 (1975).
[6]F. Califano, R. Prandi, F. Pegoraro, and S. V. Bulanov, "Nonlinear filamentation instability driven by an inhomogeneous current in a collisionless plasma," Phys. Rev. E **58**, 7837 (1998).
[7]H. Hora, "Theory of relativistic self-focusing of laser radiation in plasmas," J. Opt. Soc. Am. **65**, 882 (1975).
[8]R. Z. Sagdeev, G. I. Solov'ev, V. D. Shapiro, V. I. Shevchenko, and I. U. Yusupov, "Plasma turbulence and dissipation of a strong electromagnetic wave in the vicinity of the $n_c$ / 4 resonance," Sov. J. Exp. Theor. Phys. **55**, 74 (1982).
[9]V. P. Silin and V. T. Tikhonchuk, "Parametric plasma turbulence," Phys. Rep. **135**(1), 1 (1986).
[10]A. S. Kingsep, L. I. Rudakov, and R. N. Sudan, "Spectra of strong Langmuir turbulence," Phys. Rev. Lett. **31**, 1482 (1973).
[11]R. Dautray and J. P. Watteau, "La fusion thermonucléaire inertielle par laser. Partie 1," in *L'interaction Laser-Matière* (Commissariat à l'énergie atomique, 1993), Vol. 1.
[12]W. L. Kruer, *The Physics of Laser Plasma Interactions* (CRC Press, 2019).
[13]B. B. Afeyan and E. A. Williams, "Stimulated Raman sidescattering with the effects of oblique incidence," Phys. Fluids **28**, 3397 (1985).
[14]R. K. Follett, J. G. Shaw, J. F. Myatt, C. Dorrer, D. H. Froula, and J. P. Palastro, "Thresholds of absolute instabilities driven by a broadband laser," Phys. Plasmas **26**, 062111 (2019).
[15]M. J. Rosenberg, A. A. Solodov, W. Seka, R. K. Follett, J. F. Myatt, A. V. Maximov, C. Ren, S. Cao, P. Michel, M. Hohenberger *et al.*, "Stimulated Raman scattering mechanisms and scaling behavior in planar direct-drive experiments at the National Ignition Facility," Phys. Plasmas **27**, 042705 (2020).
[16]A. Simon, R. W. Short, E. A. Williams, and T. Dewandre, "On the inhomogeneous two-plasmon instability," Phys. Fluids **26**, 3107 (1983).
[17]J. F. Myatt, H. X. Vu, D. F. DuBois, D. A. Russell, J. Zhang, R. W. Short, and A. V. Maximov, "Mitigation of two-plasmon decay in direct-drive inertial confinement fusion through the manipulation of ion-acoustic and Langmuir wave damping," Phys. Plasmas **20**, 052705 (2013).
[18]R. K. Follett, J. G. Shaw, J. F. Myatt, J. P. Palastro, R. W. Short, and D. H. Froula, "Suppressing two-plasmon decay with laser frequency detuning," Phys. Rev. Lett. **120**, 135005 (2018).
[19]L. Hao, J. Li, W. D. Liu, R. Yan, and C. Ren, "Simulation of stimulated Brillouin scattering and stimulated Raman scattering in shock ignition," Phys. Plasmas **23**, 042702 (2016).
[20]T. Kolber, W. Rozmus, and V. T. Tikhonchuk, "Saturation of stimulated Raman scattering by Langmuir and ion-acoustic wave coupling," Phys. Fluids B **5**, 138 (1993).
[21]S. Depierreux, J. Fuchs, C. Labaune, A. Michard, H. A. Baldis, D. Pesme, S. Hüller, and G. Laval, "First observation of ion acoustic waves produced by the Langmuir decay instability," Phys. Rev. Lett. **84**, 2869 (2000).
[22]S. Depierreux, C. Labaune, J. Fuchs, D. Pesme, V. T. Tikhonchuk, and H. A. Baldis, "Langmuir decay instability cascade in laser-plasma experiments," Phys. Rev. Lett. **89**, 045001 (2002).
[23]V. E. Zakharov, "Collapse of Langmuir waves," Sov. Phys. JETP **35**, 908 (1972).
[24]M. V. Goldman, "Strong turbulence of plasma waves," Rev. Mod. Phys. **56**, 709 (1984).
[25]R. S. Craxton, K. S. Anderson, T. R. Boehly, V. N. Goncharov, D. R. Harding, J. P. Knauer, R. L. McCrory, P. W. McKenty, D. D. Meyerhofer, J. F. Myatt *et al.*, "Direct-drive inertial confinement fusion: A review," Phys. Plasmas **22**, 110501 (2015).
[26]A. G. Seaton and T. D. Arber, "Laser-plasma instabilities in long scale-length plasmas relevant to shock-ignition," Phys. Plasmas **27**, 082704 (2020).
[27]A. Colaïtis, G. Duchateau, X. Ribeyre, Y. Maheut, G. Boutoux, L. Antonelli, P. Nicolaï, D. Batani, and V. Tikhonchuk, "Coupled hydrodynamic model for laser-plasma interaction and hot electron generation," Phys. Rev. E **92**, 041101 (2015).
[28]A. R. Christopherson, R. Betti, C. J. Forrest, J. Howard, W. Theobald, J. A. Delettrez, M. J. Rosenberg, A. A. Solodov, C. Stoeckl, D. Patel *et al.*,

"Direct measurements of DT fuel preheat from hot electrons in direct-drive inertial confinement fusion," Phys. Rev. Lett. **127**, 055001 (2021).
[29]L. J. Perkins, B. G. Logan, G. B. Zimmerman, and C. J. Werner, "Two-dimensional simulations of thermonuclear burn in ignition-scale inertial confinement fusion targets under compressed axial magnetic fields," Phys. Plasmas **20**, 072708 (2013).
[30]L. J. Perkins, D. D. M. Ho, B. G. Logan, G. B. Zimmerman, M. A. Rhodes, D. J. Strozzi, D. T. Blackfield, and S. A. Hawkins, "The potential of imposed magnetic fields for enhancing ignition probability and fusion energy yield in indirect-drive inertial confinement fusion," Phys. Plasmas **24**, 062708 (2017).
[31]J. Davies, "Laser-driven magnetized liner inertial fusion on OMEGA," in APS Division of Plasma Physics Meeting Abstracts, 2018.
[32]D. H. Barnak, J. R. Davies, R. Betti, M. J. Bonino, E. M. Campbell, V. Y. Glebov, D. R. Harding, J. P. Knauer, S. P. Regan, A. B. Sefkow *et al.*, "Laser-driven magnetized liner inertial fusion on OMEGA," Phys. Plasmas **24**, 056310 (2017).
[33]J. D. Moody, B. B. Pollock, H. Sio, D. J. Strozzi, D. D.-M. Ho, C. A. Walsh, G. E. Kemp, B. Lahmann, S. O. Kucheyev, B. Kozioziemski *et al.*, "Increased ion temperature and neutron yield observed in magnetized indirectly driven d 2-filled capsule implosions on the National Ignition Facility," Phys. Rev. Lett. **129**, 195002 (2022).
[34]C. A. Walsh, J. P. Chittenden, K. McGlinchey, N. P. L. Niasse, and B. D. Appelbe, "Self-generated magnetic fields in the stagnation phase of indirect-drive implosions on the National Ignition Facility," Phys. Rev. Lett. **118**, 155001 (2017).
[35]G. Yonas, "Fusion and the Z pinch," Sci. Am. **279**, 40 (1998).
[36]S. A. Slutz, M. C. Herrmann, R. A. Vesey, A. B. Sefkow, D. B. Sinars, D. C. Rovang, K. J. Peterson, and M. E. Cuneo, "Pulsed-power-driven cylindrical liner implosions of laser preheated fuel magnetized with an axial field," Phys. Plasmas **17**, 056303 (2010).
[37]M. G. Haines, "Physics of high-density Z-pinch plasmas, by M. A. Liberman, J. S. De Groot, A. Toor and R. B. Spielman. Springer-Verlag, New York, 1999. 350 pages. ISBN 0 387 98568 9. Â£65.00, $79.95.," J. Plasma Phys. **64**, 309 (2000).
[38]C. A. Walsh, R. Florido, M. Bailly-Grandvaux, F. Suzuki-Vidal, J. P. Chittenden, A. J. Crilly, M. A. Gigosos, R. C. Mancini, G. Pérez-Callejo, C. Vlachos *et al.*, "Exploring extreme magnetization phenomena in directly driven imploding cylindrical targets," Plasma Phys. Controlled Fusion **64**, 025007 (2022).
[39]P. Y. Chang, G. Fiksel, M. Hohenberger, J. P. Knauer, R. Betti, F. J. Marshall, D. D. Meyerhofer, F. H. Séguin, and R. D. Petrasso, "Fusion yield enhancement in magnetized laser-driven implosions," Phys. Rev. Lett. **107**, 035006 (2011).
[40]C. A. Walsh, S. O'Neill, J. P. Chittenden, A. J. Crilly, B. Appelbe, D. J. Strozzi, D. Ho, H. Sio, B. Pollock, L. Divol *et al.*, "Magnetized ICF implosions: Scaling of temperature and yield enhancement," arXiv:2112.05840 (2021).
[41]M. Bailly-Grandvaux, R. Florido, C. A. Walsh, G. Pérez-Callejo, F. N. Beg, P. Bradford, M. A. Gigosos, R. C. Mancini, C. McGuffey, F. Suzuki-Vidal *et al.*, "Impact of strong magnetization in cylindrical plasma implosions with applied B-field measured via x-ray emission spectroscopy," Phys. Rev. Res. **6**, L012018 (2024).
[42]B. Srinivasan and X.-Z. Tang, "The mitigating effect of magnetic fields on Rayleigh-Taylor unstable inertial confinement fusion plasmas," Phys. Plasmas **20**, 056307 (2013).
[43]C. A. Walsh, "Magnetized ablative Rayleigh-Taylor instability in three dimensions," Phys. Rev. E **105**, 025206 (2022).
[44]R. Z. Sagdeev and V. D. Shapiro, "Nonlinear penetration of a plasma by an electromagnetic wave and nondecay mechanisms of its energy dissipation," Sov. J. Exp. Theor. Phys. **39**, 811 (1974).
[45]J. M. Dawson, V. K. Decyk, R. W. Huff, I. Jechart, T. Katsouleas, J. N. Leboeuf, B. Lembege, R. M. Martinez, Y. Ohsawa, and S. T. Ratliff, "Damping of large-amplitude plasma waves propagating perpendicular to the magnetic field," Phys. Rev. Lett. **50**, 1455 (1983).
[46]B. J. Winjum, F. S. Tsung, and W. B. Mori, "Mitigation of stimulated Raman scattering in the kinetic regime by external magnetic fields," Phys. Rev. E **98**, 043208 (2018).
[47]W. Yao, A. Higginson, J.-R. Marquès, P. Antici, K. Béard, J. Burdonov, M. Borghesi, A. Castan, A. Ciardi, B. Coleman *et al.*, "Dynamics of nanosecond laser pulse propagation and of associated instabilities in a magnetized underdense plasma," Phys. Rev. Lett. **130**, 265101 (2023).
[48]X. X. Li, R. J. Cheng, Q. Wang, D. J. Liu, S. Y. Lv, Z. M. Huang, S. T. Zhang, X. M. Li, Z. J. Chen, Q. Wang *et al.*, "Anomalous staged hot-electron acceleration by two-plasmon decay instability in magnetized plasmas," Phys. Rev. E **108**, L053201 (2023).
[49]J. F. Myatt, J. G. Shaw, R. K. Follett, D. H. Edgell, D. H. Froula, J. P. Palastro, and V. N. Goncharov, "LPSE: A 3-D wave-based model of cross-beam energy transfer in laser-irradiated plasmas," J. Comput. Phys. **399**, 108916 (2019).
[50]R. K. Follett, H. Wen, D. H. Froula, D. Turnbull, and J. P. Palastro, "Independent-hot-spot approach to multibeam laser-plasma instabilities," Phys. Rev. E **105**, L063201 (2022).
[51]R. K. Follett, J. F. Myatt, J. G. Shaw, D. T. Michel, A. A. Solodov, D. H. Edgell, B. Yaakobi, and D. H. Froula, "Simulations and measurements of hot-electron generation driven by the multibeam two-plasmon-decay instability," Phys. Plasmas **24**, 102134 (2017).
[52]T. Katsouleas and J. M. Dawson, "Unlimited electron acceleration in laser-driven plasma waves," Phys. Rev. Lett. **51**, 392 (1983).
[53]V. D. Shapiro and D. Üçer, "Shock surfing acceleration," Planet. Space Sci. **51**, 665 (2003).
[54]K. R. Carpenter, R. C. Mancini, E. C. Harding, A. J. Harvey-Thompson, M. Geissel, M. R. Weis, S. B. Hansen, K. J. Peterson, and G. A. Rochau, "Magnetic field impact on the laser heating in MagLIF," Phys. Plasmas **27**, 052704 (2020).
[55]R. K. Follett, J. G. Shaw, J. F. Myatt, D. H. Froula, and J. P. Palastro, "Multibeam absolute stimulated Raman scattering and two-plasmon decay," Phys. Rev. E **101**, 043214 (2020).
[56]H. X. Vu, D. F. DuBois, J. F. Myatt, and D. A. Russell, "Hot-electron production and suprathermal heat flux scaling with laser intensity from the two-plasmon-decay instability," Phys. Plasmas **19**, 102703 (2012).
[57]A. R. Christopherson, R. Betti, C. J. Forrest, J. Howard, W. Theobald, E. M. Campbell, J. Delettrez, M. J. Rosenberg, A. A. Solodov, C. Stoeckl *et al.*, "Inferences of hot electron preheat and its spatial distribution in OMEGA direct drive implosions," Phys. Plasmas **29**, 122703 (2022).
[58]C. S. Liu, M. N. Rosenbluth, and R. B. White, "Raman and Brillouin scattering of electromagnetic waves in inhomogeneous plasmas," Phys. Fluids **17**, 1211 (1974).
[59]F. Valentini, P. Veltri, and A. Mangeney, "Magnetic-field effects on nonlinear electrostatic-wave Landau damping," Phys. Rev. E **71**, 016402 (2005).
[60]X. X. Li, R. J. Cheng, Q. Wang, D. J. Liu, S. Y. Lv, Z. M. Huang, S. T. Zhang, Z. J. Chen, Z. Y. Xu, Q. Wang *et al.*, "Nonlinear saturation of the two-plasmon decay instability in magnetized plasmas," Phys. Rev. E **111**, 035207 (2025).
[61]S. Bolaños, M. Bailly-Grandvaux, B. J. Winjum, M. J. E. Manuel, A. Bogale, T. Filkins, D. H. Froula, R. Lee, W. Mori, F. Tsung *et al.*, "Direct evidence of the effect of a moderate external magnetic field on stimulated Raman scattering in the kinetic regime," Phys. Plasmas **32**, 092102 (2025).
[62]M. J. Rosenberg, A. A. Solodov, J. F. Myatt, W. Seka, P. Michel, M. Hohenberger, R. W. Short, R. Epstein, S. P. Regan, E. M. Campbell, T. Chapman, C. Goyon, J. E. Ralph, M. A. Barrios, J. D. Moody, and J. W. Bates, "Origins and scaling of hot-electron preheat in ignition-scale direct-drive inertial confinement fusion experiments," Phys. Rev. Lett. **120**, 055001 (2018).
[63]H. Wen, A. V. Maximov, R. Yan, J. Li, C. Ren, and F. S. Tsung, "Three-dimensional particle-in-cell modeling of parametric instabilities near the quarter-critical density in plasmas," Phys. Rev. E **100**, 041201 (2019).
[64]Y.-J. Gu, O. Klimo, V. T. Tikhonchuk, and S. Weber, "Multi-dimensional kinetic simulations of laser radiation absorption and electron acceleration in inhomogeneous underdense plasma," Nucl. Fusion **61**, 066014 (2021).
[65]D. F. Dubois, D. A. Russell, and H. A. Rose, "Saturation spectra of the two-plasmon decay instability," Phys. Rev. Lett. **74**, 3983 (1995).
[66]H. X. Vu, D. F. DuBois, D. A. Russell, and J. F. Myatt, "Hot-electron generation by 'cavitating' Langmuir turbulence in the nonlinear stage of the two-plasmon-decay instability," Phys. Plasmas **19**, 102708 (2012).
[67]R. Yan, C. Ren, J. Li, A. V. Maximov, W. B. Mori, Z.-M. Sheng, and F. S. Tsung, "Generating energetic electrons through staged acceleration in the two-plasmon-decay instability in inertial confinement fusion," Phys. Rev. Lett. **108**, 175002 (2012).
[68]E. Rovere, A. Colaïtis, R. K. Follett, and A. Casner, "Hot electron scaling for two-plasmon decay in ICF plasmas," Phys. Plasmas **30**, 042104 (2023).
[69]S. H. Cao and C. Ren, "Evolution and hot electron generation of laser-plasma instabilities in direct-drive inertial confinement fusion," Phys. Plasmas **30**, 092701 (2023).